Effects of LES Inflow Turbulence Assumptions on Wind Response of a Tall Building

Jack K. Wong[*1], Oya Mercan[1] and Paul J. Kushner[1]

[1]University of Toronto
35 St. George St., Toronto, Ontario, Canada

Abstract.   Turbulence integral lengthscale and lateral and vertical turbulence intensities are sometimes not measured in wind tunnel experiments. The resulting uncertainty in inflow conditions cascades into uncertainties in the surface pressure, drag and lift coefficients, and the wind response of tall buildings. This paper utilizes Large Eddy Simulation (LES) with a divergence-free turbulence generator to investigate a set of five inflow conditions generated using different assumptions related to building height and turbulence integral lengthscale, and the ratio between three components of turbulence intensities. The effects of the inflow assumptions on the downstream incident flow, on the surface pressure coefficient of a tall rectangular building of 1:4 width to height ratio, on drag and lift moment coefficients are all evaluated. Furthermore, an example steel-frame-tube structure is considered to investigate the effects of the inflow turbulence on its background, resonant and peak displacement response using modal analysis with gust peak factors. It is observed that distinct turbulence inflow conditions tend to converge towards similar statistical profiles downstream. However, within this envelope of convergence, a range of potential values persists, indicating significant remaining uncertainty. The inflow turbulence integral lengthscale is found to have an effect up to 13% on the peak along-wind response and 4% on the across-wind response. The lateral and vertical turbulence intensity is found to have effects of up to 13% and 24% on the two peak responses, respectively. These results highlight the importance of considering a range of inflow assumptions when conducting LES to reproduce and interpret WT results.

Keywords: Large Eddy Simulation (LES), tall building, synthetic turbulence generator, dynamic structural analysis, steel-frame-tube system

1. Introduction

Under the effects of changing climate, it is becoming increasingly crucial to analyze the impact of extreme wind events on built infrastructure such as tall buildings (Teran et al., 2022). Currently, given a design wind speed, structural engineers rely on wind tunnel (WT) testing to predict wind loads on tall buildings. However, discrepancies of up to 15% on force coefficients are commonly observed across wind tunnel tests (Irwin, 2013; Melbourne, 1980). Reproducing wind tunnel results is a complex task due to the large number of experimental variables wind loads depend on, some of which lack proper documentation. In a typical atmospheric boundary layer (ABL) WT experiment for the evaluation of wind loads on a structure, the structural model is placed at the center of a turntable in the test section. Upstream of the test section, spiral and roughness elements are placed to simulate the inflow turbulence for a set of target atmospheric boundary layer (ABL) turbulence conditions (Irwin, 1981; Song, 2017). Among these conditions, the longitudinal (along-wind) component of the mean velocity and turbulence intensity are the most crucial ones that characterize a target terrain type. To ensure good agreement between the turbulence statistics in the WT and that of the ABL, calibration needs to be performed by adjusting the sizes and layout of the roughness elements. While the vertical profiles of the mean and turbulence intensity of the longitudinal velocity are often measured and documented in WT tests for verification of the inflow characteristics, the methodology and the location of these measurement are not always documented. In general, there are two types of WT inflow definitions: the approach flow and the incident flow (Blocken et al., 2008). The approach flow corresponds to the wind flow upstream of the turntable with or without the building model while the incident flow corresponds to the wind flow in an empty domain at the center of the turntable. Numerical simulations of the WT show that the approach flow and incident flow can sometimes show noticeable discrepancies (Abu-Zidan & Nguyen, 2023; Lamberti et al., 2018; Melaku & Bitsuamlak, 2024). The lack of documentation of these important aspects of the configuration of WT experiments leads to uncertainty in the background turbulence conditions. Additionally, other secondary inflow characteristics, e.g. lateral components of turbulence intensities, integral lengthscales, and turbulence decay characteristics, are often considered less important and are neither measured nor documented.

Although the fluctuating pressure on a structure shows strong dependence on longitudinal mean velocity and turbulence intensities as described by the quasi-steady assumption (Holmes, 2015), the lateral (cross-wind)

---

*Corresponding author, Ph.D. Candidate
 E-mail: kittai.wong@mail.utoronto.ca

components of turbulence are also expected to affect wind loads by altering the wind angle of attack and disturbing body-generated flow phenomena such as separations, re-attachments, and vortex shedding (Hatanaka & Tanaka, 2008; Peil & Behrens, 2007). While there is much previous work on the effects of inflow turbulence on the force distribution on a cylinder (Hu & Li, 2012; Zhang et al., 2023; Zhao et al., 2021), the lateral components of turbulence are rarely studied, especially for settings that evaluate wind force on a tall building in an ABL-like environment. Quantifying the effects of secondary inflow characteristics is important for understanding the discrepancies among WT test results (Huang et al., 2007; Irwin, 2013; Melbourne, 1980) and between WT and numerical simulation results.

With advances in high-performance-computing, Computational Fluid Dynamics (CFD) methods are becoming commonly used to study the wind effects on tall buildings (Abu-Zidan et al., 2021; Agrawal et al., 2022; Dagnew & Bitsuamlak, 2014; Elshaer et al., 2016; Melaku & Bitsuamlak, 2024; Meng et al., 2023; Teran et al., 2022). While WT is still considered as the most reliable method for obtaining wind loads acting on buildings, CFD methods offers some advantages over WT testing. First, all inputs and geometry of the CFD are well-defined with high precision. This allows parametric study of any variable in a controlled manner. Second, CFD provides high-resolution results for the flow fields both temporally and spatially, which are difficult to measure in a WT due to limitations and interference effects of the instruments. While currently it is challenging to reproduce WT results with CFD, it serves as a great tool for studying flow phenomena, and therefore it is important to reduce the gap between CFD and WT.

Large Eddy Simulation (LES) has been shown to predict wind loads on tall buildings with reasonable accuracy when proper set-up is applied (Melaku & Bitsuamlak, 2024; Thordal, Bennetsen, Capra, & Koss, 2020; Thordal, Bennetsen, Capra, Kragh, et al., 2020). While currently it is still computationally expensive to simulate the WT along with the test-section, the development in synthetic turbulence generators enables preparation of divergence-free inflow turbulence for specified turbulence characteristics with affordable computational cost (Kim et al., 2013; Melaku & Bitsuamlak, 2021; Poletto et al., 2011). While previous researches mainly focus on the longitudinal turbulence statistics (Aly, 2014; Zhang et al., 2023), the effects of the lateral and vertical component of turbulence on the response of tall buildings have rarely been studied. State-of-the-art synthetic turbulence generators provide a means to study the effects of inflow turbulence statistics on a building model in a controlled manner, by generating time-histories of the inflow turbulence using different assumptions for the relationship between unknown inflow quantities.

In the present work, LES is used to study the effects of inflow lateral turbulence intensities and integral length scales on the wind loads acting on a tall rectangular building. Five inflow time-histories are generated by assuming different relationships between the building

height and the integral lengthscale, and between the three components of turbulence intensities. Their effects on the surface wind pressure coefficient, and on local and overall drag and lift forces are then evaluated. Furthermore, to investigate the resulting effects on the dynamic response of the building, a steel structure is considered, and the peak displacement response is obtained based on the five different inflow assumptions.

In the following, Section 2 details the CFD configuration and methodology, and the inflow assumptions used for this study. Section 3 presents the effects of inflow assumptions on wind forces on a rigid body. Section 4 introduces the example tall-building steel structure and studies the effects of inflow assumptions on its response. Section 6 concludes the study with a discussion on implications and future work.

2. CFD Methods

This section describes the CFD set-up and the corresponding wind tunnel configuration. It also summarizes the set of inflow conditions used and discusses the discrepancies between turbulence statistics of the inflow and those of the incident flow.

2.1 Tokyo Polytechnic University (TPU) Aerodynamic Database

The present study utilizes the High-rise Buildings with Rectangular/Square Plan dataset from the Tokyo Polytechic University (TPU) Aerodynamic Database (TPU, 2012). The dimensions of the test-section of the ABL wind tunnel are not included with the dataset. The width and height of the test-section are assumed to be 2.0m and 1.8m based on (Tanaka et al., 2012). The wind tunnel test case selected for preparing the LES simulation has a 0.1m wide square-section building model with a breadth: depth: height ratio of 1:1:4 and a model scale of 1:400, an exposure factor of 1/4 and a wind angle of attack of 0°. This leads to a blockage ratio of 1.11%. The dataset consists of time-histories of 400 pressure taps, distributed uniformly across the four lateral surfaces of the building model, sampled at 1000Hz with a sampling period of 32.8s. The vertical profiles of mean velocity and longitudinal turbulence intensity of incoming flow are provided. However, the lateral and vertical turbulence intensities and the integral lengthscales are not included with the dataset.

3.2 CFD Set-up

OpenFOAM v2006 is utilized in the current study to generate the mesh and perform the LES simulations. The LES simulation is conducted in the same geometric scale (1:400) as the TPU experiment on the building model of 0.1m width (W) and 0.4m height (H). Like the WT, the computational domain has a cross-section of 2.0m width and 1.8 m tall, resulting in the same blockage ratio of 1.11%. following the recommendations from CFD guidelines (Franke et al., 2007), the length of the computational domain was set as 10m, and the building center is located 6.25H downstream of the inlet plane and
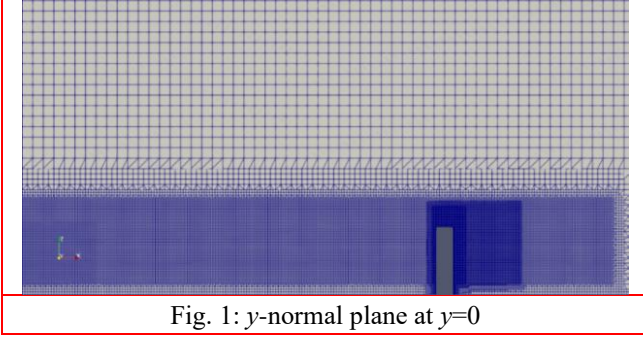
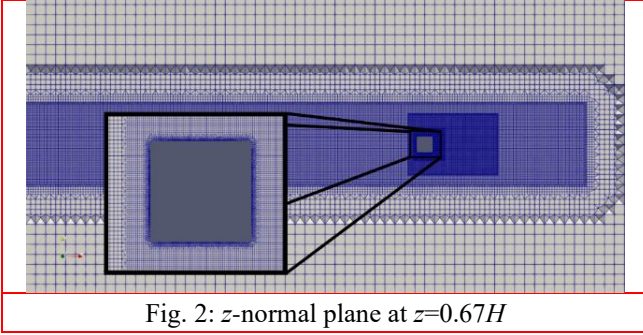18.75H from the outlet plane.

Fig. 1: *y*-normal plane at *y*=0

Fig. 2: *z*-normal plane at *z*=0.67*H*

The mesh consists of 8 million hexahedra cells with regional refinement and inflation layers around the building model. The background mesh is formed with cubical cells with length of 0.156H. The background mesh is then subdivided into smaller cubical cells to form the regional regions. To preserve the inflow turbulence, the region around and in between the building model and the inlet plane is subdivided three times (corresponding to length of 0.0195H). Close to the building model, the cells are further refined to resolve the body-generated turbulence (with cell lengths of 0.00975H in the near-wake and 0.00487H close to the building surface) and with transition regions adjacent to the background mesh. On the building surface, 11 inflation layers are inserted with an overall height of 0.00385H, leading to an average y^+ value of ~2. Near the ground, the cell size was kept at 0.039H to maintain an average y^+ value ~30. Fig. 1 and Fig. 2 show the mesh configuration in the y-normal plane at *y*=0 and the *z*-normal plane at *z*=0.67*H*, respectively.

The top and side planes of the computational domain employ symmetric boundary conditions, while at the outlet plane, zero gradient is imposed. At the inlet plane, time-varying turbulence inflow is used (details in section 2.3). Both the ground and the building surface have no-slip conditions with wall functions to model the effects of turbulence viscosity near the wall.

The standard Spalding smooth wall function (Spalding, 1961) is applied to the building surface to provide a wall constraint on the turbulent viscosity based on the calculated y^+ value by the following empirical relationship:

$$y^+ = u^+ + \frac{1}{E}\left[\exp\left(\kappa u^+ - 1 - \kappa u^+ - 0.5(\kappa u^+)^2 - \frac{1}{6}(\kappa u^+)^3\right] \tag{1}$$

where u^+ is the velocity near wall in wall units, E is a roughness parameter with a value of 9.8, and κ is the von Karman constant with a value of 0.41.

To maintain the shape of the inflow velocity profile, a rough wall function derived from the Schumann-Grotzbach equation is applied to the ground surface:

$$u_\tau = \frac{\kappa}{\ln\left(\frac{z_p + z_0}{z_0}\right)}\sqrt{\langle U(z_p,t)\rangle \widetilde{u_\iota}(x_p,y_p,z_p,t)} \tag{2}$$

where u_τ is the friction velocity, x_p, y_p, z_p are the coordinates of the cell centroid adjacent to the wall, z_0 is the aerodynamic roughness length, $\langle U \rangle$ is the instantaneous flow velocity averaged over the layer of cells adjacent to the wall and $\widetilde{u_\iota}$ is the instantaneous filtered velocity.

Pressure Implicit with Splitting of Operator (PISO) algorithm (Issa, 1986) with the wall-adapting local eddy-viscosity (WALE) model (Nicoud & Ducros, 1999) is used for the LES simulation. The WALE model has been shown to perform well form modelling the flow around tall buildings (Melaku & Bitsuamlak, 2024; Wang & Chen, 2020). Each simulation ran with 0.0005-second timesteps for 15 seconds, with the first 5 seconds discarded. Each simulation took approximately 3200 core-hours to complete. The empty domain utilizes a time-step of 0.005-second, and each simulation took approximately 320 core-hours to complete. The simulations were conducted on the high-performance cluster, Niagara, hosted by SciNet in Toronto, Canada (Loken et al., 2010; Ponce et al., 2019).

2.3. Turbulence Inflow Generation and Comparison with Incident Flow

The divergence-free inflow turbulence generator using spectral representation (DFSR) method (Melaku & Bitsuamlak, 2021) was employed to prepare the inflow for this study. The DFSR method employs the FFT technique to generate velocity time-series based on the factorized cross-power spectral density (CPSD) matrix prescribed to satisfy the target inflow characteristics. The implementation at https://github.com/abiyfantaye/DFSR (Melaku, 2023) is used for the current study. This implementation employs a

Table 1. Summary of the inflow statistics for the sensitivity study

Cases	U_H	I_{uH}	I_v/I_u	I_w/I_u	L_u^x/H	L_v^x/L_u^x	L_w^x/L_u^x
a) Base case					2		
b) low L			0.78	0.55	1		
c) high L	10.46 m/s	14%			4	0.3	0.25
d) low lateral I			0.39	0.275	2		
e) high lateral I			1	1			

2D velocity-potential-based divergence-free correction procedure with mass flow rate correction. For simplicity, each of the three components of velocity is generated independently to reduce computational cost.

The inflow longitudinal mean velocity and turbulence intensity profiles are calibrated to match with the profiles used in the TPU WT test. In this study, five turbulence conditions are numerically generated based on different assumptions on the unknown turbulence quantities: the base case (Case a), low- and high- integral lengthscale ("low-L", Case b) and "high-L", Case c) as well as low- and high-lateral and vertical turbulence intensities ("low-lateral-I", Case d and "high-lateral-I", Case e). In the base case, the lateral and vertical turbulence intensities, I_v and I_w are assumed to be 0.78 and 0.55 of the longitudinal intensity I_u based on (ESDU, 1985). The longitudinal integral lengthscale L_u^x is assumed to be $2H$ and the lateral and vertical integral lengthscale L_v^x and L_w^x, are assumed to be 0.3 and 0.25 of the longitudinal lengthscale. The "low-L" and "high-L" cases consider halving and doubling the longitudinal integral lengthscale from the base case, while the "low-lateral-I" case and the "high-lateral-I" case consider halving and lateral and vertical turbulence intensities and setting them equals to the longitudinal turbulence intensity respectively. Table 1 summarizes the inflow conditions used for each case.

The mean velocity profiles for the five cases are shown in Fig. 3, calculated at the inlet (dash-lines) and at the tentative building location in an empty domain (solid-lines). All the profiles match well with the measurements of the WT experiment, reflecting that the provided rough wall function on the ground surface is compatible with the inflow.

The turbulence integral lengthscales are computed by applying the Taylor's frozen eddy hypothesis with the method of first zero-crossing of autocorrelation and shown in Figure 4. While the integral lengthscale at the inlet plane was calibrated to match with the assumed profiles, the downstream profiles calculated at the tentative building location can vary significantly. This may be caused by the interaction between the generated flow fields and dissipation of physically incompatible turbulence (Patruno & De Miranda, 2020). The inherent variability of integral
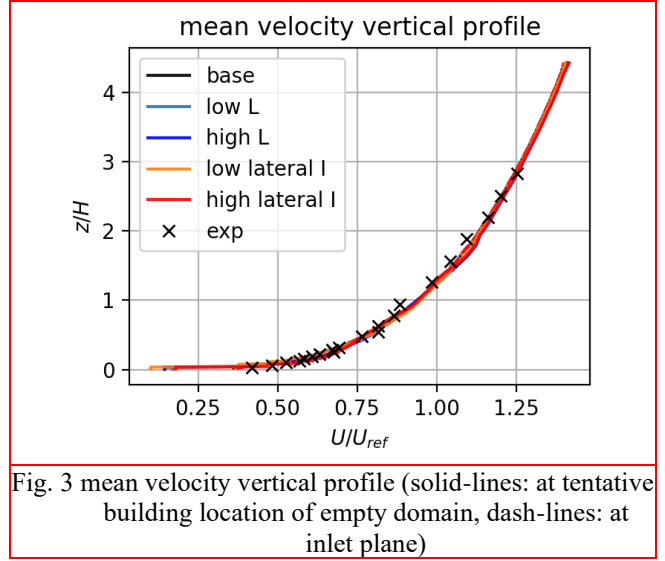

Fig. 3 mean velocity vertical profile (solid-lines: at tentative building location of empty domain, dash-lines: at inlet plane)

timescale in turbulence flow from one point to another observed in (Lamberti et al., 2018) may also plays a role. Near the ground ($z < 0.3H$), the computed lengthscale shows large variation even within a simulation case, which can be attributed to the break-down of the Taylor's frozen eddy hypothesis due to the low convective velocity. For the base case, the integral lengthscale profiles at the tentative building location are larger than those at inlet in general, reflecting the filtering and dissipation of smaller scale eddies.

By changing the inflow integral lengthscale by a significant amount (Case b and Case c), the downstream lengthscale tends to restore towards the downstream lengthscale profiles as observed in the base case (Fig. 4). This is expected as the LES solver tends to filter out small-scale eddies and convert large-scale eddies to smaller-scale eddies. Despite the reduction of the change, changing the inflow lengthscales still leads to a net change of lengthscale observed at the building location. The lengthscales at the inlet are also found to have an effect on the turbulence intensities. By halving the integral lengthscale (from Case a to Case b), the longitudinal turbulence intensity at the building location reduces by roughly 2.5% of the mean velocity while the lateral and vertical turbulence show no
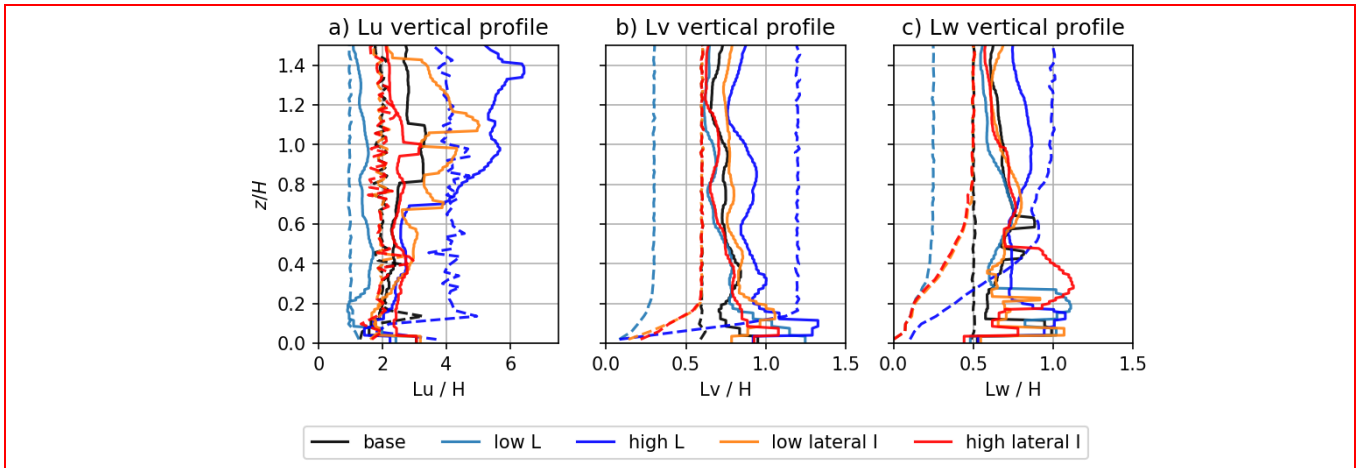

Fig. 4: Integral lengthscale vertical profiles (solid-lines: incident flow at tentative building location of empty domain, dash-lines: at inlet plane)
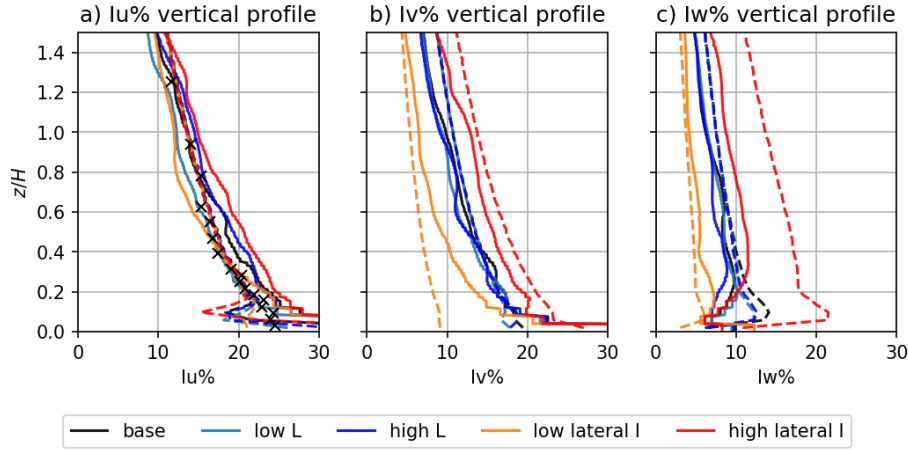
Fig 5: turbulence intensity vertical profiles (solid-lines: incident flow at tentative building location of empty domain, dash-lines: at inlet plane)

significant changes (Fig. 5). By doubling the integral lengthscale (from Case a to Case c), the longitudinal turbulence intensity increases slightly by <1% of the mean velocity and the vertical turbulence profile decreases slightly.

The profiles for the three components of turbulence intensity are shown in Fig. 5. At the inlet plane, all cases have similar longitudinal turbulence intensity vertical profiles (Fig. 5a). At the building location, the longitudinal turbulence intensity of the base case increases slightly by roughly by 2.5% of the mean velocity for $z < 0.7H$, while the lateral turbulence intensity vertical profile exhibits regions with increased intensity and regions with decreased intensity, while the vertical turbulence intensity profile decreases. This may indicate that for the base case, part of the energy in lateral and vertical turbulence is converted into longitudinal velocity fluctuations. By changing the inflow lateral and vertical turbulence intensities, the downstream turbulence profiles tend to rebalance towards the ratio of $I_u : I_v : I_w$ of approximately 1:0.75:0.5 as observed in the base case and the literature on boundary layer flow on a flat plate (Inoue, 2012) and atmospheric boundary layer (ESDU, 1985), leading to a reduced I_u profile when the lateral and vertical turbulence intensities are lowered and an increased I_u profile when the counterpart components are increased. At the building location, Case d) leads to a turbulence ratio of 1:0.6:0.35 and Case e) leads to a ratio of 1:0.8:0.55, where a net change in the lateral and vertical turbulence profiles is still observed.

3. Effects of inflow assumptions on wind force

In this section, the overall base drag and lift forces and overturning moments, as well as the mean and standard deviation of the surface pressure coefficients, are evaluated to study the effects of the differences in the prescribed inflow conditions.

3.1 Surface pressure contours

The pressure coefficient C_p on the building surface is defined as follows:

$$C_p = \frac{p - p_0}{\frac{1}{2}\rho V_H^2} \quad (3)$$

where p is the surface pressure, p_0 is the reference pressure at the inlet, ρ is density of air (1.21 kg/m^3) and V_H is the reference velocity at the building height at inlet.

Fig. 6 shows the contour of time-averaged value pressure coefficient $\overline{C_p}$ for the front, right, back and left surfaces of the building model. The base case (Case a) shows good agreement on the front face with WT, except for the near-ground region where $\overline{C_p}$ is slightly larger (by ~0.1). This can be attributed to the general good agreement in the mean velocity inflow vertical profile. Near the ground, the velocity experiences larger fluctuation relative to the mean, resulting in larger uncertainty. On the side and leeward surfaces, the magnitudes of the negative $\overline{C_p}$ are underestimated by the base case (by ~0.1). This can be attributed to the under-prediction of vortex shedding strength due to the resolution limit of the simulation. Fig. 7 shows the temporal standard deviation (STD) contours of C_p. The STD are overestimated for the front and side surfaces (by ~10%) and around the edge of the leeward surface. The overestimation of STD in the front surface indicates an overprediction of turbulence intensity and this is consistent with the profile at the tentative building location calculated in an empty domain. This may compensate with the effects of under-resolved fluctuation of vortex shedding.

Reducing the inflow integral lengthscale (Case a to Case b) leads to slight reduction in the magnitude of $\overline{C_p}$ on the leeward surface while the $\overline{C_p}$ contours on other surfaces show no significant change. The STD values show an overall reduction for all surfaces. Increasing the inflow integral lengthscale (Case c), however, leads to slight reduction in the magnitude of $\overline{C_p}$ only on the side surface while the front surface experiences increased STD values and the side surfaces experience slight reduction in STD.

The STD of C_p on the front surface correlates with the inflow lengthscale as the reverse pressure gradient around the windward surface filters out smaller eddies. Similar trend is observed for the leeward surface. No clear correlation is observed for C_p STD on the side surfaces, suggesting that the lengthscale have little effect on the C_p fluctuation on the side surface caused by body-generated vortex shedding dynamics.

Reducing the lateral and vertical turbulence intensity at the inlet (Case d) leads to a slight increase in $\overline{C_p}$ on the front face and less negative values for the side and leeward surfaces. Increasing the lateral and vertical turbulence intensities (Case e) shows little effects on the frontal surface $\overline{C_p}$, while more negative $\overline{C_p}$ is observed for the side and leeward surfaces. The magnitude of negative $\overline{C_p}$ is related to the mean strength the circulation within the region of flow separation. For flow around 3D square cylinder on a flat plate, it was found that increased oncoming turbulence intensity converts spanwise vortex shedding from in-phase to out of phase, leading to more coherent flow structures (Inoue, 2012). The same correlation is observed in the LES results. The STD C_p shows positive correlation with the inflow turbulence, as predicted by the quasi-steady assumption, except for leeward surface, on which the STD C_p seems to decrease for both cases.

3.2   Local force coefficients

The local force coefficients $C_{fD}(z)$ and $C_{fL}(z)$ are obtained by integrating the drag and lift force around the perimeter of the building at elevation z and normalizing by the reference dynamic pressure force as follows:

$$C_{fD}(z) = \dfrac{D(z)}{\frac{1}{2}\rho V_H^2 W}$$	(4)
$$C_{fL}(z) = \dfrac{L(z)}{\frac{1}{2}\rho V_H^2 W}$$	(5)
where D is the drag force and L is the lift force.	

The mean and standard deviation of $C_{fD}(z)$ and $C_{fL}(z)$ over time are computed and shown in Fig. 8. Consistent with the pressure coefficient contour plots, the mean local drag coefficient $\overline{C_{fD}}$ are underestimated for all of the cases due to the under-prediction of the leeward negative pressure. The local force coefficients aggregate the pressure along the building perimeter and therefore, it filters out spatially uncorrelated fluctuations with small lengthscales relative to the building width. The STD of C_{fD} shows positive correlation with the inflow integral lengthscale and turbulence intensities throughout the building height, except for $z/H < 0.4$ of the low-turbulence case in which little difference is observed. While from previous results for the pressure coefficient in Fig. 7, the STD for the low-lateral turbulence case shows significantly smaller values for the front surface, the insensitivity in STD of C_{fD} profile may be explained by the increased lengthscale that accompanied with the low vertical turbulence intensity as observed in Fig. 5, offsetting the effects of turbulence intensity.
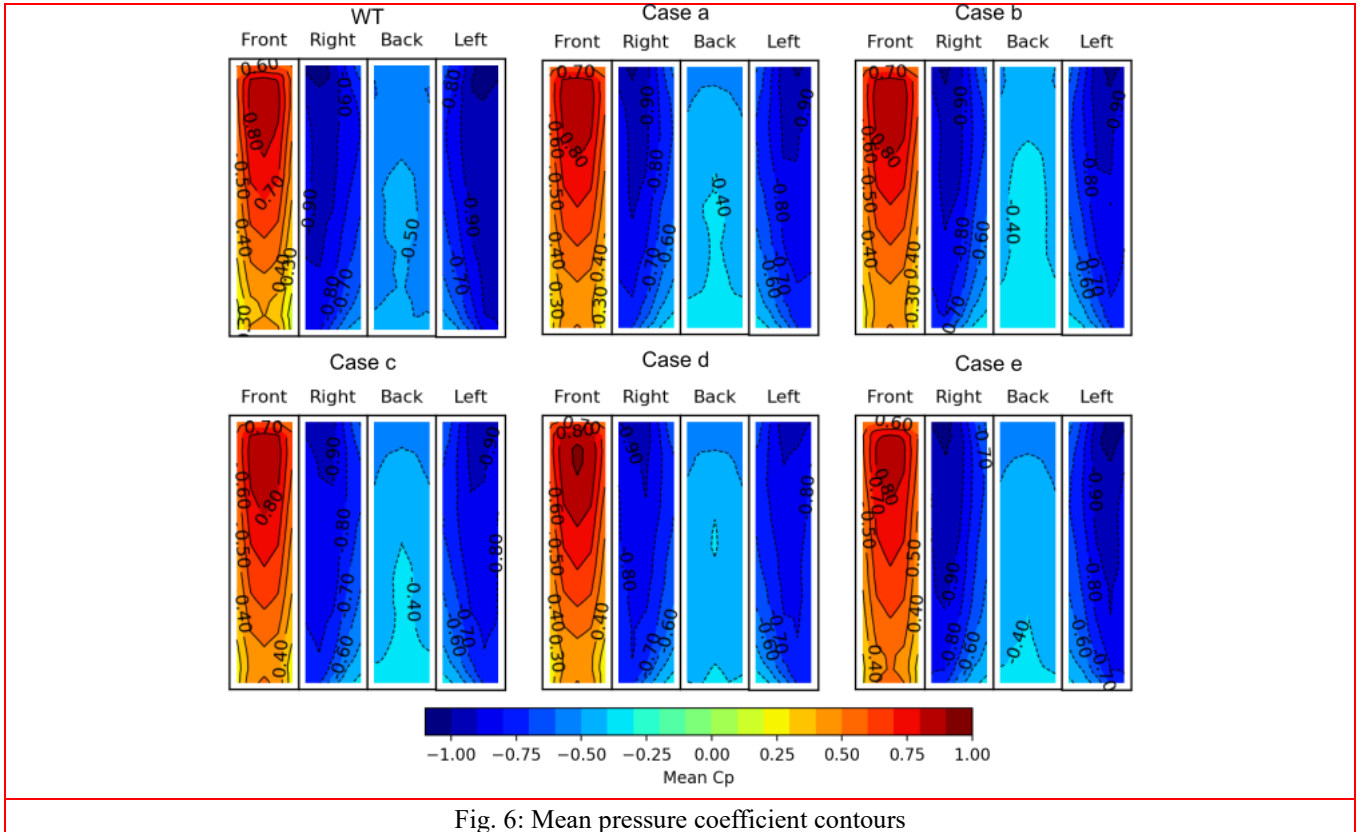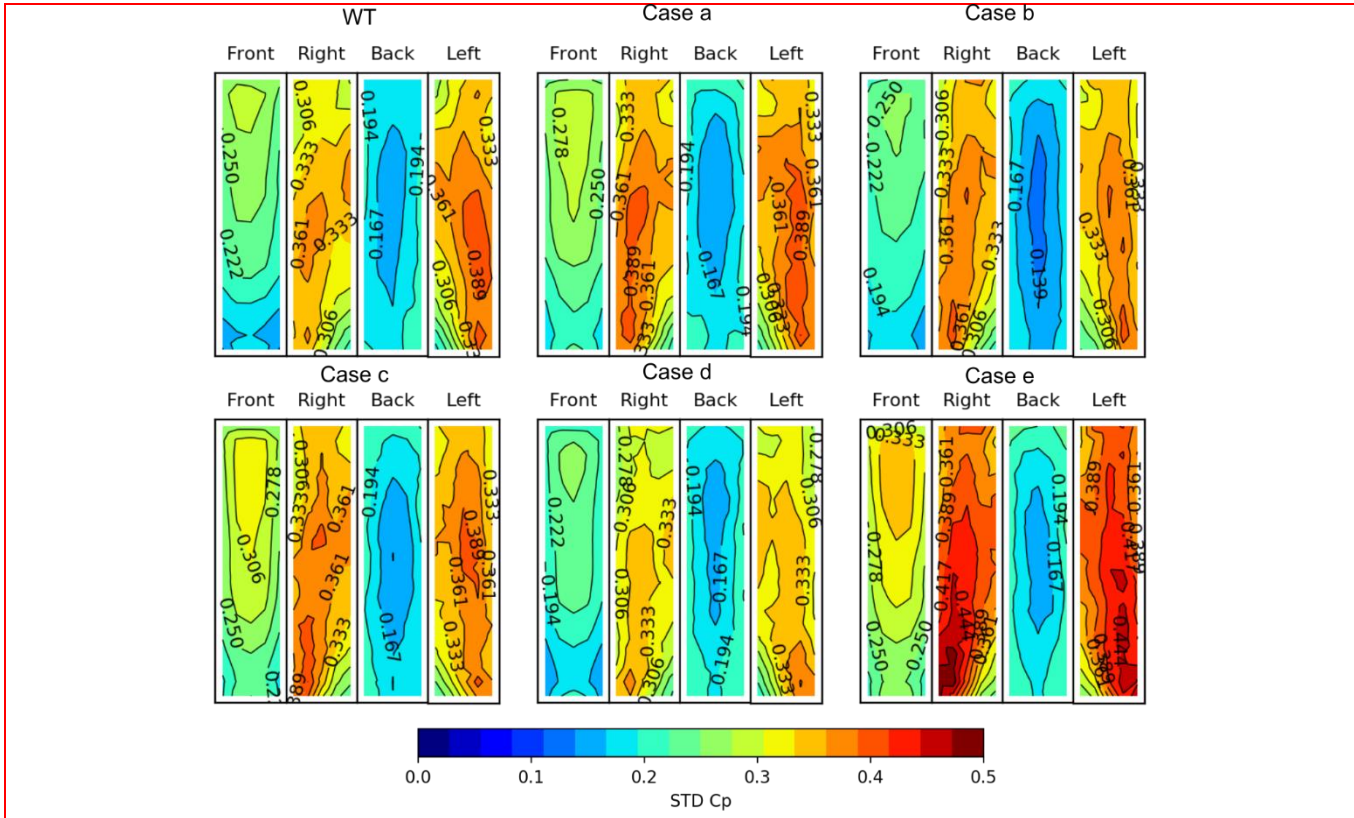

Fig. 6: Mean pressure coefficient contours

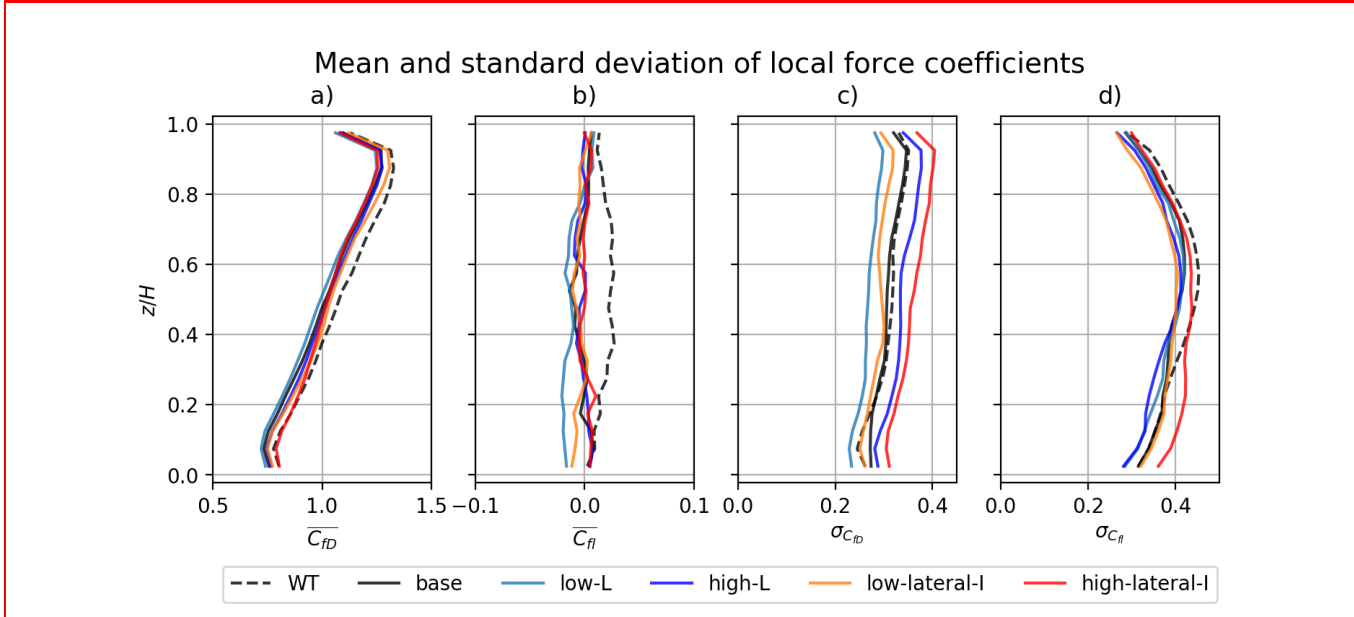Fig. 7: Standard deviation pressure coefficient contours

Fig. 8: Local force coefficients along building height

3.3. Drag and lift coefficients

The drag and lift force coefficients (C_{FD} and C_{FL}) are computed by integrating the surface pressure force in the x- and y- directions respectively and normalizing the net force by the product of projected building area normal to the flow direction and the dynamic pressure corresponding to the reference velocity. The drag and lift moment coefficients (C_{MD} and C_{ML}) are computed similarly by integrating the

moment along x- and y- directions and normalizing the net moment by an additional characteristic length H.

The mean and the standard deviation of the coefficients are tabulated in Table 2 and Table 3 along with the percentage error when compared to the WT measurements. In general, the percentage error of the force coefficients is similar to those of the corresponding moment coefficients with the exception for the STD of C_{FL} and C_{ML} of Case d. This reflects that the lift force may be underestimated in

the upper part of the building for this case. While the mean C_{MD} are underestimated for all five cases, they are within 6% of the WT measurements.

Reducing the turbulence lengthscale (Case b) tends to increase the error slightly. This is accompanied by a significant reduction in the fluctuation in C_{MD} (from 0.143 to 0.119), while the fluctuation in C_{ML} does not change significantly. On the other hand, increasing the turbulence lengthscale (Case c) leads to a slight increase in mean C_{MD} and a significant increase in the STD of C_{MD}. While changing the turbulence lengthscale would also lead to a change in the downscale turbulence intensity, Case c results in similar I_u profiles as the base case. This highlights the significant effects of inflow lengthscale on the fluctuation C_{MD}, which controls the characteristic eddy size and the coherency of the pressure force on the building surface. Both cases lead to a slight reduction in the fluctuation of C_{ML}.

Reducing the lateral and vertical turbulence intensities (Case d) lead to a slight increase in the mean C_{MD} and a slight reduction in the fluctuation of C_{MD} and C_{ML} (-5% and -1.2%). In contrast, increasing the lateral and vertical turbulence intensities (Case e) leads to significant and slight increase in the fluctuation of C_{MD} and C_{ML}, respectively (+18% and +2.5%).

The power spectral densities of the force and moment coefficients normalized by the STD of WT coefficients divided by the frequency is shown in Fig. 9. The profiles are smoothed using Welch's method for clarity. The force spectra show similar shape as the moment spectra. It is observed that the high lateral turbulence intensity and high integral lengthscale cases leads to overestimation of the fluctuating C_{MD} in the low frequency regions. A deficit around reduced frequency of 0.02 is also observed for all cases. While the fluctuation in C_{ML} is dominated by body-generated vortex shedding, slight effects are observed by altering the inflow turbulence. Increasing the lateral turbulence level leads to a slightly broader peak while reducing the lateral turbulence level leads to a sharper peak.
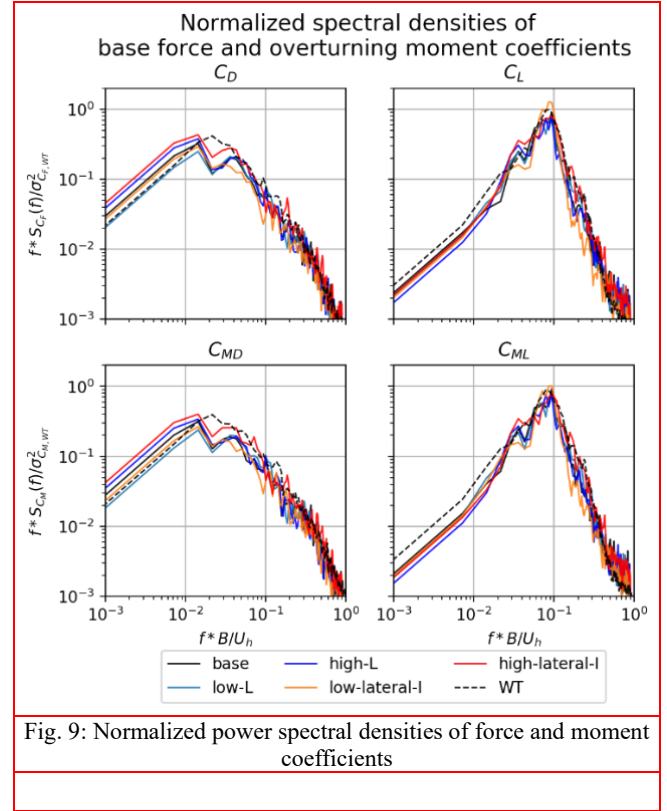

Fig. 9: Normalized power spectral densities of force and moment coefficients

Table 2. Mean of drag and lift force and moment coefficients.

| Cases | Mean (% error) | | | |
	C_{FD}	C_{FL}	C_{MD}	C_{ML}
WT	1.068	0.018	0.582	0.010
a) base	1.006 (-6%)	-0.001 (-105%)	0.551 (-5%)	-0.000 (-105%)
b) low-L	0.987 (-8%)	-0.011 (-161%)	0.541 (-7%)	-0.003 (-134%)
c) high L	1.018 (-5%)	-0.001 (-107%)	0.555 (-5%)	-0.001 (-112%)
d) low-lateral-I	1.035 (-3%)	-0.005 (-127%)	0.566 (-3%)	-0.002 (-119%)
e) high-lateral-I	1.023 (-4%)	0.002 (-91%)	0.551 (-5%)	0.001 (-94%)

Table 3. Standard deviation of drag and lift force and moment coefficients.

| Cases | STD (% error) | | | |
	C_{FD}	C_{FL}	C_{MD}	C_{ML}
WT	0.262	0.33	0.142	0.174
a) base	0.267 (2%)	0.300 (-8%)	0.143 (0%)	0.160 (-8%)
b) low-L	0.223 (-15%)	0.291 (-11%)	0.119 (-16%)	0.157 (-10%)
c) high-L	0.300 (15%)	0.288 (-12%)	0.161 (13%)	0.155 (-11%)
d) low-lateral-I	0.256 (-3%)	0.310 (-5%)	0.136 (-5%)	0.158 (-9%)
e) high-lateral-I	0.315 (20%)	0.316 (-3%)	0.169 (19%)	0.164 (-6%)

4. Effects of inflow assumptions on the response of a tall building

In this section, an example 40-storey high-rise building is introduced for linear structural dynamic analysis to study the effect of the inflow assumptions on the dynamic response of the structure.

4.1. Steel-framed-tube structure

The building selected is based on the work from (Ricci et al., 2018). The structure from (Ricci et al., 2018) is modified to have a 1:1 floor plan aspect ratio and to have the same height as the full-scale height of the building model used in CFD study. The prototype building has dimensions of 40m (width) x 40m (breadth) x 160m (height) and a storey-height of 4m. The building utilizes a steel-framed-tube system which consists of an outer ring and an inner ring (core) of columns of steel box-section to resist external lateral loads. The inner core has dimensions of 8m x 8m. The columns are spaced at 2m on the outer ring. The storeys are divided into 5 levels and the steel box-sections are designed for each level. The dimensions of the steel box-sections are tabulated in Table 4. At each floor-level, the columns are connected by deep spandrel plates of 1.2m depth and 40mm thick. A rigid diaphragm is assumed and a floor load of 16kPa is provisioned in additional to the self-weight of the steel-framed-tube system. Figure 10 shows the layout of the steel-framed-tube building.

The structure was modelled with Rhino®-Grasshopper (Robert McNeel & Associates, 2023) and Altair S-Frame (Altair Inc., 2023). Modal analysis was performed with S-Frame to find the fundamental modes of the structure. Fig. 11 shows the first three fundamental modes. The first two modes have fundamental frequency of 0.165Hz. The structure is symmetrical about the x- and y- axes, and therefore the two first two modes have the same fundamental frequency. The torsional mode has a higher fundamental frequency of 0.277 Hz.

Table 4. Dimensions of the sections of the structural elements

Level	Core elements			Framed tube elements		
	w (m)	h (m)	t (m)	w (h)	h (m)	t (m)
1	0.7	0.7	0.18	0.5	0.5	0.12
2	0.7	0.7	0.14	0.5	0.5	0.10
3	0.7	0.7	0.1	0.5	0.5	0.08
4	0.7	0.7	0.08	0.5	0.5	0.06
5	0.7	0.7	0.04	0.5	0.5	0.04

*Note: *w*: outer width, *h*: outer height, *t*: thickness

4.2. Dynamic response of wind

The dynamic response was evaluated using the method described in (Boggs & Dragovich, 2006). Considering a N-degree-of-freedom (NDOF) system subjected to harmonic loading with frequency ω and amplitude defined by a Nx1 vector $\boldsymbol{F_0}$. The equations of motion can be formulated as a system of equations as follows:

$$\mathrm{M}\ddot{x} + C\dot{x} + Kx = \boldsymbol{F_0}\cos(\omega t)$$	(6)
where $\boldsymbol{x}$, $\dot{\boldsymbol{x}}$ and $\mathbf{x}$ are the displacement, velocity, and acceleration vectors, M is the mass matrix, C is the damping matrix and K is the stiffness matrix	

The system of equation can be solved by expressing the displacement vector as the sum of N orthogonal eigenvectors weighted by the generalized coordinate $\boldsymbol{q}$:

$$\boldsymbol{x} = \sum_{j=1}^{N} q_j \boldsymbol{\phi_j}$$	(7)
where $\boldsymbol{\phi_j}$ is the mode shape of mode j	

Utilizing the orthogonality of modes, the system of equations can be decoupled into individual SDOF systems in q_j for each mode j.

$$\mathrm{M_j}\ddot{q}_j + C_j\dot{q}_j + K_j q_j = F_j\cos(\omega t)$$	(8)
where $\mathrm{M_j}$, C_j, K_j and F_j are the generalized mass, damping coefficient, stiffness and force for mode j	

The solution to equation (8) is given as:

$$q_j = |H_j(\omega)|\frac{F_j}{K_j}\cos(\omega t)$$	(9)
$$H_j(\omega) = \frac{1}{\sqrt{\left[1-\left(\frac{\omega}{\omega_j}\right)^2\right]^2 + \left[2\xi\frac{\omega}{\omega_j}\right]^2}}$$	(10)
where ξ is the damping ratio, $|H(\omega)|^2$ is referred as the mechanical admittance function	

The displacement can then be computed using equation (7). Given a mode j, the time-history of generalized wind force can be computed for the lift and drag force. The fluctuating portion of the wind force can then be expressed in frequency domain with spectral density function S_{Fj} to use equation 9. The standard deviation of the combined response can be computed from the following:

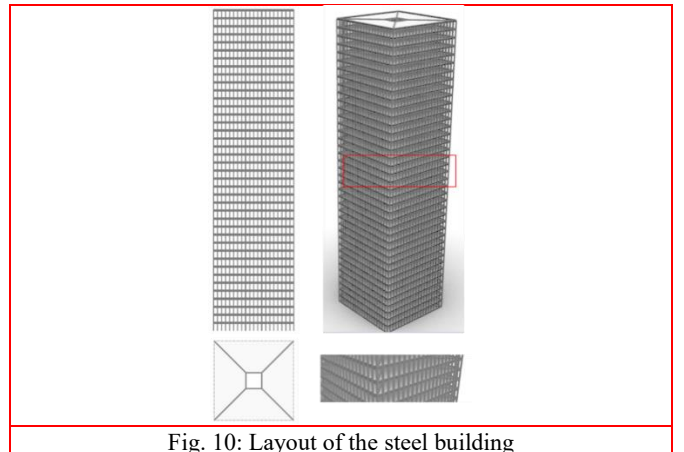| $$\sigma_{x,j} = \frac{\boldsymbol{\phi_j}}{K_j}\sqrt{\int_0^{\infty} S_{Fj}(\omega)|H_j(\omega)|^2\, df}$$	(11)

Fig. 10: Layout of the steel building

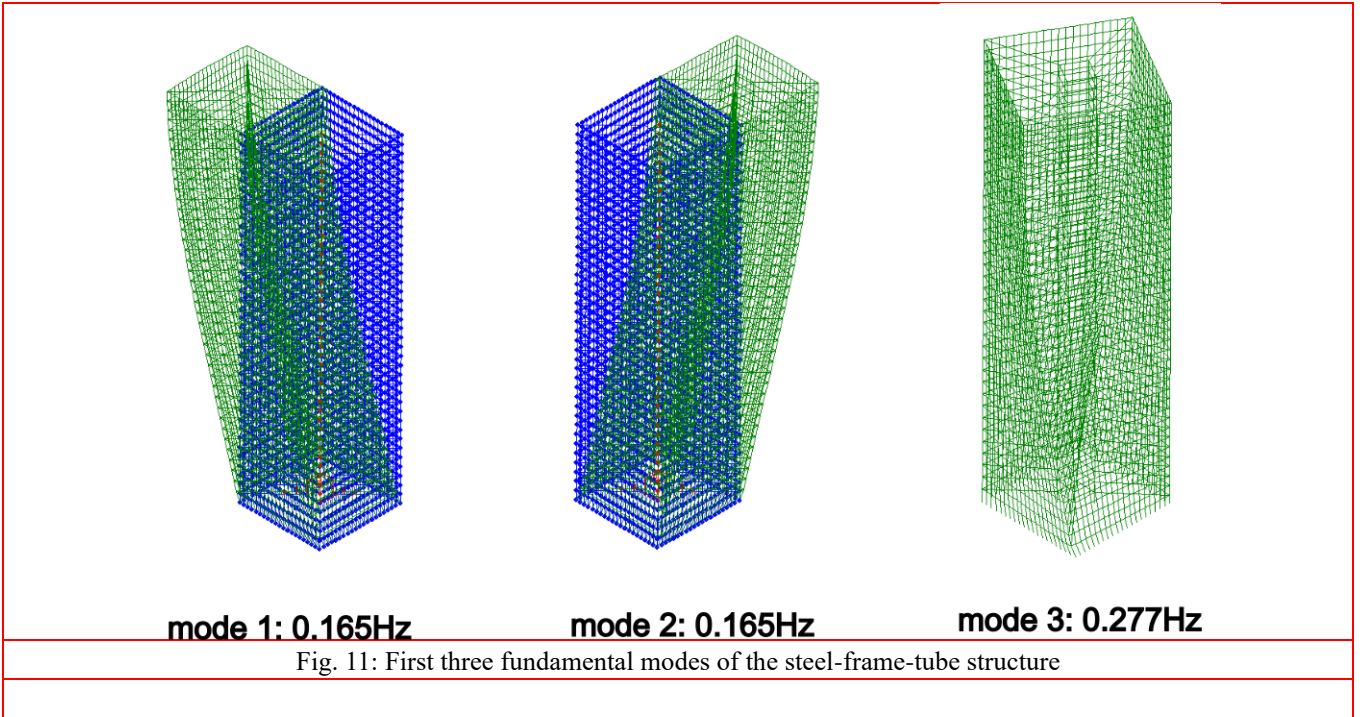mode 1: 0.165Hz   mode 2: 0.165Hz   mode 3: 0.277Hz

Fig. 11: First three fundamental modes of the steel-frame-tube structure

In wind engineering, the response is typically decomposed into background response and resonant response as the two show different characteristics. The background response $\sigma_{x,b}$ is defined by the response without mechanical amplification, and it can be calculated with equation (11) by setting $\left|H_j(\omega)\right|^2$ to 1. The resonant response can then be obtained by the following:

$$\sigma_{x,r} = \sqrt{\sigma_x^2 - \sigma_{x,b}^2} \qquad (12)$$

The peak value of the fluctuating response $\hat{x}$ can then be estimated using gust peak factors g_0 and g_1:

$$\hat{x} = \bar{x} + \sqrt{\left(g_0\sigma_{x,b}\right)^2 + \left(g_1\sigma_{x,r}\right)^2} \qquad (13)$$

For this study, g_0 is taken as 3.5 and g_1 is calculated using the following expression (Davenport, 1961):

$$g_1 = \sqrt{2 ln f_1 T} + \frac{0.577}{\sqrt{2 ln f_1 T}} \qquad (14)$$

Where f_1 is the first-mode fundamental frequency, T is the time period for which the peak is estimated, taken as 3600 seconds in this study

For the building used in this study, the first two modes have a mass participation factor of 0.86. To simplify the analysis, only the first two modes are considered. The design wind speed is assumed to be 30m/s at the building height.

4.3. Along-wind response

The mean, background, resonant and peak responses in the along-wind direction are calculated for the steel-frame-tube structure subjected to each of the different inflow conditions (Fig 12). Fig. 12c shows that all five inflow

conditions lead to a similar mean vertical response profile similar to the response calculated from WT measurements. This shows that despite the small discrepancy in the mean drag profile, the error in the resultant mean response is small compared to the inherent fluctuation of the response. The base case leads to similar background response compared to WT, while the resonant response is underestimated at the roof by ~15%. This may be explained by the underestimation of leeward pressure fluctuation, which has relatively higher frequency corresponding to the vortex shedding frequency and closer to the resonant frequency of the building. The underestimation in resonant response leads to underestimation of peak response (97mm compared to 105mm in WT, -8% error).

By reducing the inflow lengthscale, background response is significantly reduced while the resonant response shows a slight decrease. The peak response is calculated to be 91mm, showing an error of -13%. In contrast, increasing the inflow lengthscale leads to slight increase in the background response and a slight decrease in the resonant response. The changes compensate for each other, and the peak response was estimated to be 97mm.

By reducing the lateral and vertical inflow turbulence, the effects are similar to reducing inflow lengthscale. The background response shows a significant decrease while the resonant response shows a slight decrease. This leads to a peak response of 93mm (-11% error). Increasing turbulence leads to significant increases in both the background response and resonant response, resulting in overestimation in both of the responses. The peak response was calculated to be 106mm (+1% error).

4.4. Across-wind response

The across-wind responses are shown in Fig. 13. All five simulations result in lower background response than that computed from WT measurements. This is linked to the

under-resolved vortex shedding intensity. This also leads to underestimation of the resonant response as the vortex frequency (~0.075Hz) is close to the building fundamental frequency (0.165Hz) compared to the frequency content of the background turbulence. The peak response for the base case is computed to be 92mm compared to 115mm from WT measurements, resulting in -20% error. The error is large compared to the percentage error in STD of C_{ML}. This suggests that the base case underestimates the fluctuation of lift force in higher frequency range.

Reducing the inflow lengthscale leads to a slight increase in background response and a substantial increase in the resonant response. This is opposite to the trend for surface pressure fluctuation. This suggests that while the pressure fluctuation for individual points is reduced, there is an increase in lift force in higher frequency range close to the building fundamental frequency. The peak displacement at the roof is calculated to be 102mm (-11% error). On the other hand, increasing the lengthscale leads to slight reduction in both background and displacement responses. The peak roof displacement is calculated to be 88mm (-23% error).
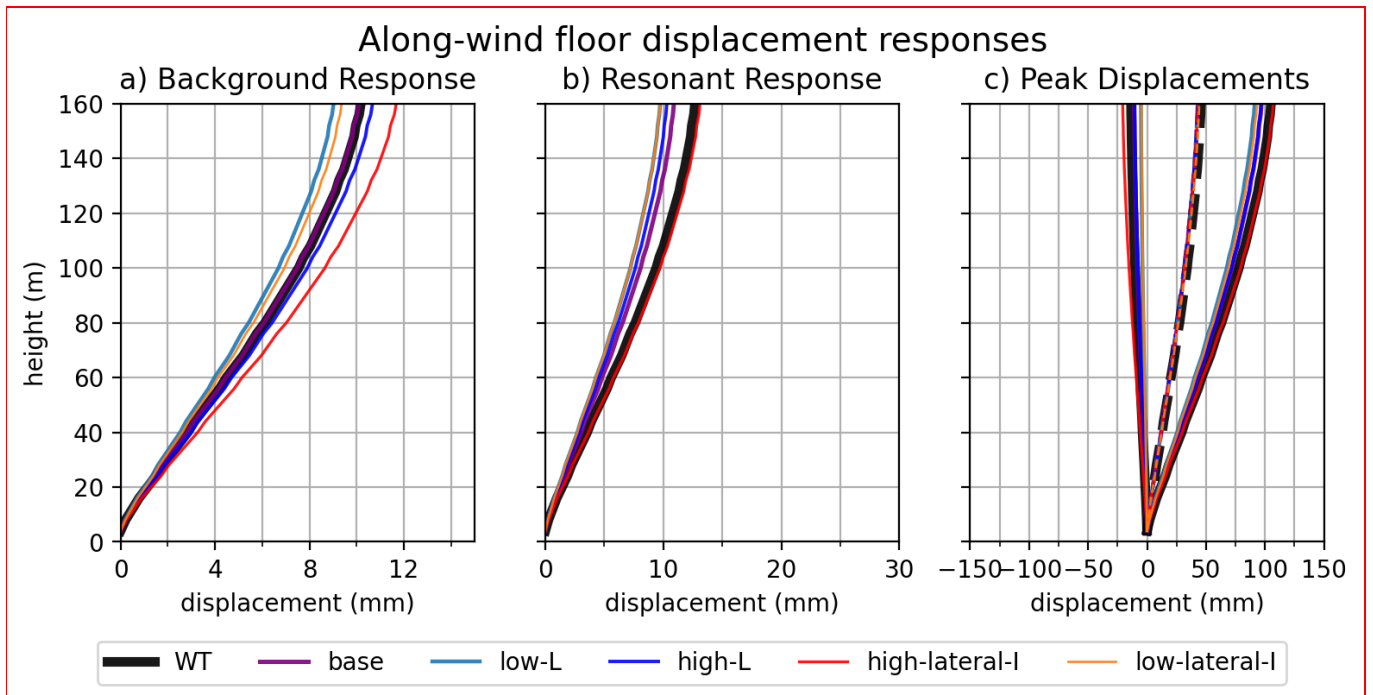

Fig. 12: Along-wind floor displacement responses (dash-line: mean response)
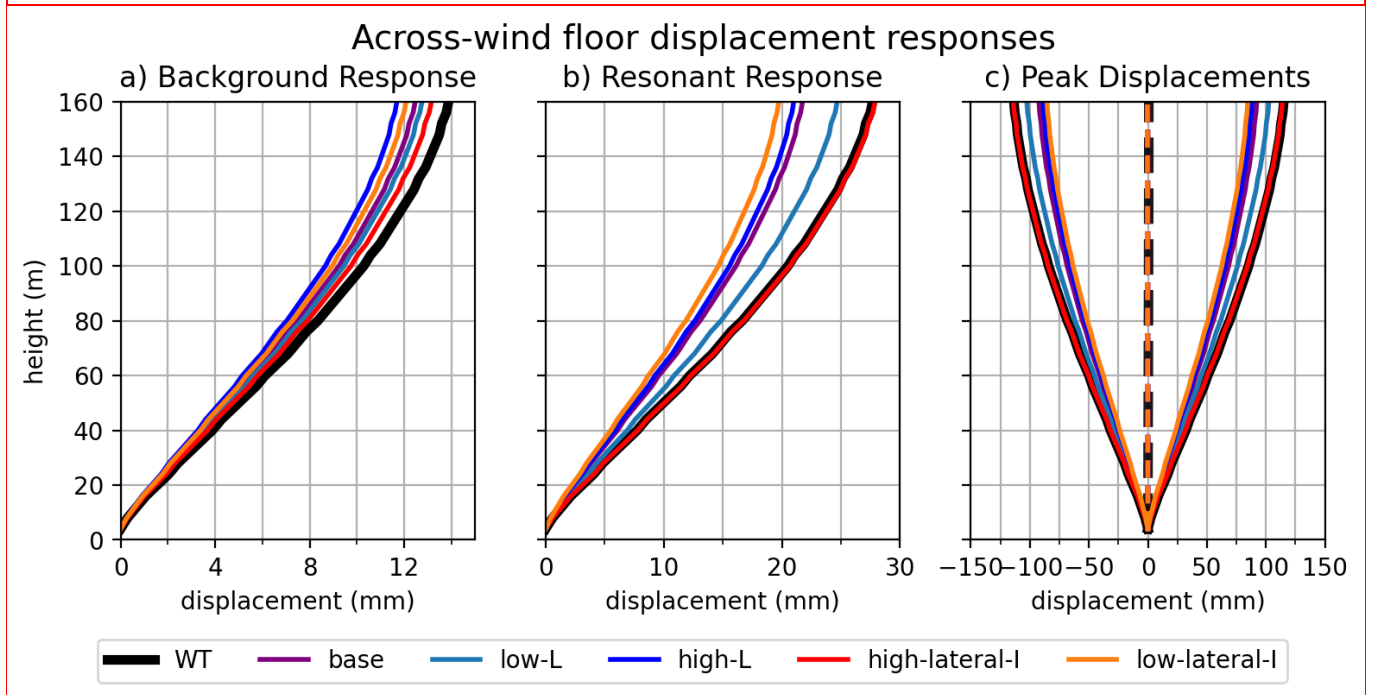

Fig. 13: Standard deviation pressure coefficient contours

By reducing the lateral and vertical turbulence intensities, the displacement response decreased from 28mm to 20mm, and the resonant response decreased from 14mm to 12mm, resulting in a peak response of 84mm (-27% error). Increasing the turbulence intensities led to the opposite effects, the displacement and resonant responses increased to 13mm and 28mm respectively and the resulting peak response is calculated to be 114mm (-1% error). The increase in lateral and vertical turbulence intensities led to increased frequency content in the higher frequency range and it offsets the error caused by under-estimating vortex shedding intensity, leading to reduced overall error for the displacement response.

5. Conclusions and future work

In wind tunnel tests, the vertical profile of integral lengthscale and lateral and vertical turbulence intensities are sometimes not measured, and even when they are, they are often not documented. In this study, five turbulence conditions are numerically generated based on different assumptions on the unknown turbulence quantities: the base case, high- and low- integral lengthscale as well as high- and low- lateral and vertical turbulence intensities. The effects of the inflow conditions on the incident flow statistics, surface pressure coefficient on the building model, local force coefficients, overall lift and drag force and moment coefficients as well as the displacement response of an example building are studied through CFD simulations. It was found that:

- The base case generated with conventional assumptions on inflow turbulence led to around 10% error on temporal standard deviation of pressure coefficient and overall drag and moment coefficients compared to the WT results. However, the peak displacement responses are underestimated by 8% in the along-wind direction and 20% in the across-wind direction.

- By changing the inflow integral lengthscale or the lateral and vertical turbulence intensities from the base case, the downstream incident turbulence tends to re-adjust towards a range of compatible turbulence statistics by damping out the imposed change. The L_u^x, L_v^x, L_w^x tend to restore to around ratio $3H$, $0.75H$ and $0.75H$ and I_u, I_v and I_w tends to restore to between 1:0.6:0.35 and 1:0.8:0.55.

- Changing the inflow assumptions on integral lengthscales and lateral and vertical turbulence does not have significant effects on the time-averaged pressure coefficient, drag and moment coefficients and displacement response on the steel building.

- Reducing the integral lengthscale led to a reduction in the temporal standard deviation of surface pressure, local and overall drag and lift coefficients.

The peak along-wind response is reduced by 6% while the peak across-wind response shows an increase of 11%.

- Increasing the integral lengthscale led to an increase in the temporal standard deviation of surface pressure on the windward surface, local and overall drag coefficients, while a reduction is observed for the surface pressure on the side surface, local and overall lift coefficients. The peak along-wind response decreased by 1% while the peak across-wind response decreased by 4%.

- Reducing the lateral and vertical turbulence intensities led to a reduction in the temporal standard deviation of surface pressure on the front and side surfaces, local and overall drag and lift coefficients, while an increase is observed for the pressure coefficients on the leeward surface. The peak along-wind and across-wind responses are reduced by 13% and 4% respectively.

- Increasing the lateral and vertical turbulence intensities led to an increase in the temporal standard deviation of surface pressure on the windward and side surfaces, local and overall drag and lift coefficients. The peak response along-wind and across-wind responses increased by 10% and 24% respectively.

This paper has demonstrated the effects of inflow assumptions on the integral lengthscale as well as lateral and vertical turbulence intensities, on the wind loads and displacement response of a tall building. While the CFD resolution remains to be an important factor in resolving and computing the across-wind response to capture the vortex shedding strength and higher-frequency fluctuations, inflow assumptions are found also to have significant effects on the dynamic response of the structure. This highlights the importance of measuring the vertical profiles of integral lengthscales as well as the lateral and vertical turbulence intensities during WT experiments. If the turbulence inflow assumptions differ from the atmospheric boundary layer turbulence at the site location for a building, CFD may provide a means to study the effects of the differences such that a correction can be made.

This study only examines three components of lengthscale and three turbulence intensities, while there are additional parameters for the inflow turbulence. These include velocity lengthscales in the across-wind and vertical directions, which are typically represented by coherency decay coefficients, and Reynolds shear stresses. This study can be extended further to include the coherency decay coefficients and the Reynolds stress tensor. For the dynamic response, this study can be extended by considering higher-order mode effects. Also, longer-duration CFD simulations can be performed to study the how the inflow conditions affect the peak events obtained from LES.

Acknowledgments

References

Abu-Zidan, Y., Mendis, P., & Gunawardena, T. (2021). Optimising the computational domain size in CFD simulations of tall buildings. *Heliyon*, *7*(4), e06723. https://doi.org/10.1016/j.heliyon.2021.e06723

Abu-Zidan, Y., & Nguyen, K. (2023). A machine learning approach for calibrating ABL profiles in large-eddy simulations. *Journal of Wind Engineering and Industrial Aerodynamics*, *232*, 105277. https://doi.org/10.1016/j.jweia.2022.105277

Agrawal, S., Wong, J. K., Song, J., Mercan, O., & Kushner, P. J. (2022). Assessment of the aerodynamic performance of unconventional building shapes using 3D steady RANS with SST k-ω turbulence model. *Journal of Wind Engineering and Industrial Aerodynamics*, *225*, 104988. https://doi.org/10.1016/j.jweia.2022.104988

Altair Inc. (2023). *Model, Analyze, and Design Any Structure | Altair S-FRAME*. Model, Analyze, and Design Any Structure | Altair S-FRAME. https://altair.com/s-frame

Aly, A. M. (2014). Influence of Turbulence, Orientation, and Site Configuration on the Response of Buildings to Extreme Wind. *The Scientific World Journal*, *2014*, 1–15. https://doi.org/10.1155/2014/178465

Blocken, B., Stathopoulos, T., & Carmeliet, J. (2008). Wind Environmental Conditions in Passages between Two Long Narrow Perpendicular Buildings. *Journal of Aerospace Engineering*, *21*(4), 280–287. https://doi.org/10.1061/(ASCE)0893-1321(2008)21:4(280)

Boggs, D., & Dragovich, J. (2006). The Nature of Wind Loads and Dynamic Response. *Special Publication*, *240*, 15–44. https://doi.org/10.14359/18290

Dagnew, A. K., & Bitsuamlak, G. T. (2014). Computational evaluation of wind loads on a standard tall building using les. *Wind and Structures, An International Journal*, *18*(5), 567–598. Scopus. https://doi.org/10.12989/was.2014.18.5.567

Davenport, A. G. (1961). *A statistical approach to the treatment of wind loading on tall masts and suspension bridges* [University of Bristol]. http://ethos.bl.uk/OrderDetails.do?uin=uk.bl.ethos.555378

Elshaer, A., Aboshosha, H., Bitsuamlak, G., El Damatty, A., & Dagnew, A. (2016). LES evaluation of wind-induced responses for an isolated and a surrounded tall building. *Engineering Structures*, *115*, 179–195. https://doi.org/10.1016/j.engstruct.2016.02.026

ESDU. (1985). Characteristics of atmospheric turbulence near the ground. Part 2: Single point data for strong winds (neutral atmosphere). In *Unknown*. https://ui.adsabs.harvard.edu/abs/1985catn.rept......

Franke, J., Baklanov, A., Hellsten, A., Schlünzen, H., & Carissimo, B. (2007). *Best Practice Guideline for the CFD Simulation of Flows in the Urban Environment: COST Action 732 Quality Assurance and Improvement of Microscale Meteorological Models*.

Hatanaka, A., & Tanaka, H. (2008). Aerodynamic admittance functions of rectangular cylinders. *Journal of Wind Engineering and Industrial Aerodynamics*, *96*(6–7), 945–953. https://doi.org/10.1016/j.jweia.2007.06.048

Holmes, J. D. (2015). *Wind loading of structures* (Third edition). CRC Press.

Hu, G., & Li, Q. S. (2012). *The effects of freestream turbulence on wind-induced responses of tall buildings*.

Huang, S., Li, Q. S., & Xu, S. (2007). Numerical evaluation of wind effects on a tall steel building by CFD. *Journal of Constructional Steel Research*, *63*(5), 612–627. https://doi.org/10.1016/j.jcsr.2006.06.033

Inoue, M. (2012). *Large-Eddy Simulation of the Flat-plate Turbulent Boundary Layer at High Reynolds numbers*.

Irwin, H. P. A. H. (1981). The design of spires for wind simulation. *Journal of Wind Engineering and Industrial Aerodynamics*, *7*(3), 361–366. https://doi.org/10.1016/0167-6105(81)90058-1

Irwin, H. P. A. H. (2013). *Wind tunnel testing of high-rise buildings: An output of the CTBUH Wind Engineering Working Group* (1st edition). Routledge. https://doi.org/10.4324/9781315879529

Issa, R. I. (1986). Solution of the implicitly discretised fluid flow equations by operator-splitting. *Journal of Computational Physics*, *62*(1), 40–65. https://doi.org/10.1016/0021-9991(86)90099-9

Kim, Y., Castro, I. P., & Xie, Z.-T. (2013). Divergence-free turbulence inflow conditions for large-eddy simulations with incompressible flow solvers. *Computers & Fluids*, *84*, 56–68. https://doi.org/10.1016/j.compfluid.2013.06.001

Lamberti, G., García-Sánchez, C., Sousa, J., & Gorlé, C. (2018). Optimizing turbulent inflow conditions for large-eddy simulations of the atmospheric boundary layer. *Journal of Wind Engineering and Industrial Aerodynamics*, *177*, 32–44. https://doi.org/10.1016/j.jweia.2018.04.004

Loken, C., Gruner, D., Groer, L., Peltier, R., Bunn, N., Craig, M., Henriques, T., Dempsey, J., Yu, C.-H., Chen, J., Dursi, L. J., Chong, J., Northrup, S., Pinto, J., Knecht, N., & Zon, R. V. (2010). *SciNet: Lessons Learned from Building a Power-efficient Top-20 System and Data Centre*. *256*, 012026. https://doi.org/10.1088/1742-6596/256/1/012026

Melaku, A. F. (2023). *Abiyfantaye/DFSR: DFSR is a synthetic inflow turbulence generation method tailored to computational wind engineering applications*. https://github.com/abiyfantaye/DFSR/tree/main

Melaku, A. F., & Bitsuamlak, G. T. (2021). A divergence-free inflow turbulence generator using spectral representation method for large-eddy simulation of ABL flows. *Journal of Wind Engineering and Industrial Aerodynamics*, *212*, 104580. https://doi.org/10.1016/j.jweia.2021.104580

Melaku, A. F., & Bitsuamlak, G. T. (2024). Prospect of LES for predicting wind loads and responses of tall buildings: A validation study. *Journal of Wind Engineering and Industrial Aerodynamics*, *244*, 105613. https://doi.org/10.1016/j.jweia.2023.105613

Melbourne, W. H. (1980). Comparison of measurements on the CAARC standard tall building model in simulated model wind flows. *Journal of Wind Engineering and Industrial Aerodynamics*, *6*(1), 73–88. https://doi.org/10.1016/0167-6105(80)90023-9

Meng, M., Tamura, T., Katsumura, A., & Fugo, Y. (2023). LES application to wind pressure prediction for tall building on complex terrain. *Journal of Wind Engineering and Industrial Aerodynamics*, *242*, 105582. https://doi.org/10.1016/j.jweia.2023.105582

Nicoud, F., & Ducros, F. (1999). Subgrid-scale stress modelling based on the square of the velocity gradient tensor. *Flow, Turbulence and Combustion*, *62*(3), 183–200. Scopus. https://doi.org/10.1023/A:1009995426001

Patruno, L., & De Miranda, S. (2020). Unsteady inflow conditions: A variationally based solution to the insurgence of pressure fluctuations. *Computer Methods in Applied Mechanics and Engineering*, *363*, 112894. https://doi.org/10.1016/j.cma.2020.112894

Peil, U., & Behrens, M. (2007). Aerodynamic admittance models for buffeting excitation of high and slender structures. *Journal of Wind Engineering and Industrial Aerodynamics*, *95*(2), 73–90. https://doi.org/10.1016/j.jweia.2006.05.007

Poletto, R., Revell, A., Craft, T. J., & Jarrin, N. (2011). DIVERGENCE FREE SYNTHETIC EDDY METHOD FOR EMBEDDED LES INFLOW BOUNDARY CONDITIONS. *Proceeding of Seventh International Symposium on Turbulence and Shear Flow Phenomena*, 1–6. https://doi.org/10.1615/TSFP7.2040

Ponce, M., van Zon, R., Northrup, S., Gruner, D., Chen, J., Ertinaz, F., Fedoseev, A., Groer, L., Mao, F., Mundim, B. C., Nolta, M., Pinto, J., Saldarriaga, M., Slavnic, V., Spence, E., Yu, C.-H., & Peltier, W. R. (2019). Deploying a Top-100 Supercomputer for Large Parallel Workloads: The Niagara Supercomputer. *Proceedings of the Practice and Experience in Advanced Research Computing on Rise of the Machines (Learning)*, 1–8. https://doi.org/10.1145/3332186.3332195

Ricci, M., Patruno, L., Kalkman, I., de Miranda, S., & Blocken, B. (2018). Towards LES as a design tool: Wind loads assessment on a high-rise building. *Journal of Wind Engineering and Industrial Aerodynamics*, *180*, 1–18. https://doi.org/10.1016/j.jweia.2018.07.009

Robert McNeel & Associates. (2023). *Rhinoceros 3D*. Www.Rhino3d.Com. https://www.rhino3d.com/

Song, P. (2017). *Simulation of Atmospheric Boundary Layer in an Open-Loop Wind Tunnel Using Spire-Roughness-Element Technique* [ProQuest Dissertations Publishing]. https://search.proquest.com/docview/1987971962

Spalding, D. B. (1961). A Single Formula for the "Law of the Wall." *Journal of Applied Mechanics*, *28*(3), 455–458. https://doi.org/10.1115/1.3641728

Tanaka, H., Tamura, Y., Ohtake, K., Nakai, M., & Chul Kim, Y. (2012). Experimental investigation of aerodynamic forces and wind pressures acting on tall buildings with various unconventional configurations. *Journal of Wind Engineering and Industrial Aerodynamics*, *107–108*, 179–191. https://doi.org/10.1016/j.jweia.2012.04.014

Teran, A. S., Agrawal, S., Naderian, H., Wong, J. K., Song, J., Mercan, O., Kushner, P. J., Mardukhi, J., & Zhang, X. (2022). Towards a Computational Workflow for Studying the Effects of Climate Change on Wind Loads on High-Rise Buildings in Urban Areas. *Atmosphere-Ocean*, *60*(2), 124–140. https://doi.org/10.1080/07055900.2022.2061412

Thordal, M. S., Bennetsen, J. C., Capra, S., & Koss, H. H. H. (2020). Towards a standard CFD setup for wind load assessment of high-rise buildings: Part 1 – Benchmark of the CAARC building. *Journal of Wind Engineering and Industrial Aerodynamics*, *205*, 104283. https://doi.org/10.1016/j.jweia.2020.104283

Thordal, M. S., Bennetsen, J. C., Capra, S., Kragh, A. K., & Koss, H. H. H. (2020). Towards a standard CFD setup for wind load assessment of high-rise buildings: Part 2 – Blind test of chamfered and rounded corner high-rise buildings. *Journal of Wind Engineering and Industrial*

Aerodynamics, *205*, 104282. https://doi.org/10.1016/j.jweia.2020.104282

TPU. (2012). *TPU Aerodynamic Database—High-rise Buildings with Rectangular/Square Plan*. https://db.wind.arch.t-kougei.ac.jp/aerodynamic/experiment/highrise/

Wang, Y., & Chen, X. (2020). Simulation of approaching boundary layer flow and wind loads on high-rise buildings by wall-modeled LES. *Journal of Wind Engineering and Industrial Aerodynamics*, *207*, 104410. https://doi.org/10.1016/j.jweia.2020.104410

Zhang, Y., Cao, S., Cao, J., & Wang, J. (2023). Effects of turbulence intensity and integral length scale on the surface pressure on a rectangular 5:1 cylinder. *Journal of Wind Engineering and Industrial Aerodynamics*, *236*, 105406. https://doi.org/10.1016/j.jweia.2023.105406

Zhao, C., Wang, H., Zeng, L., Alam, Md. M., & Zhao, X. (2021). Effects of oncoming flow turbulence on the near wake and forces of a 3D square cylinder. *Journal of Wind Engineering and Industrial Aerodynamics*, *214*, 104674. https://doi.org/10.1016/j.jweia.2021.104674